Experimental measurement of interparticle acoustic radiation force in the Rayleigh limit

Abhishek Ray Mohapatra, Shahrokh Sepehrirahnama, and Kian-Meng Lim[*]

Department of Mechanical Engineering, National University of Singapore, Singapore 119077

Acoustophoresis is a form of contact-free particle manipulation in microfluidic devices. The precision of manipulation can be enhanced with better understanding of the acoustic radiation force. In this paper we present the measurements of interparticle radiation force between a pair of polystyrene beads in the Rayleigh limit. The study is conducted for three different sizes of beads and the experimental results are of the same order of magnitude when compared with theoretical predictions. However, the experimental values are larger than the theoretical values. The trend of a decrease in the magnitude of the interparticle radiation force with decreasing particle size and increasing center-to-center distance between the particles is also observed experimentally. The experiments are conducted in the specific scenario where the pair of beads are in close proximity, but not in contact with each other, and the beads are approaching the pressure nodal plane with the center-to-center line aligned perpendicular to the incident wave. This scenario minimizes the presence of the primary radiation force, allowing accurate measurement of the interparticle force. The attractive nature of the interparticle force is observed, consistent with theoretical predictions.

I. INTRODUCTION

Among various techniques for particle manipulation in microfluidics and lab-on-a-chip devices, acoustophoresis has become popular in recent years. Acoustophoresis utilizes the acoustic radiation force to move the particles in a host fluid due to a difference in acoustic contrast factor (which is dependent on density and compressibility) of the particle and the host fluid. Due to its versatility and contact-free nature, acoustic radiation force has been used for handling biological cells and particles [1]. To better understand the nature of the acoustic radiation force, various theoretical and experimental studies have been conducted over the years. Besides the primary radiation force experienced by particles due to the incident wave, the particles in close proximity interact with one another. Hence, the total radiation force experienced by an individual particle is the sum of the primary radiation force and the interparticle radiation force (also known as the secondary radiation force) due to the neighboring particles. Therefore, the study of interparticle radiation force is vital in predicting the trajectory of particles and quantifying the phenomenon of particle agglomeration in a densely populated suspension of particles.

The pioneering work on the radiation force was conducted by Lord Rayleigh. King [2] studied the radiation force acting on a single rigid sphere in a fluid medium and derived an analytical formula to calculate the primary radiation force. Subsequently, many studies were conducted to calculate the radiation force on the objects in both inviscid and viscous fluid media. Yosioka and Kawasima [3] derived an analytical expression for the primary radiation force on a compressible sphere due to a plane wave in inviscid fluid. The viscosity of the fluid medium considerably affects the primary radiation force on both rigid and compressible spheres [4,5]. Settnes and Bruus [6] gave an analytical expression for the radiation force acting on a single compressible sphere in a viscous fluid medium using multipole expansion up to dipole terms. Using high-order multipole expansion, Sepehrirahnama *et al.* [7] developed a numerical scheme to accurately calculate the primary radiation force for a sphere in viscous fluid, without the restriction of the small size of the sphere compared to the wavelength. Recently, Johnson *et al.* [8] experimentally verified that the viscosity of the fluid will cause higher acoustic radiation force on a particle in a traveling wave. The importance of the viscosity effect of the fluid is substantial while calculating the acoustic radiation force and should not be neglected. To handle objects of arbitrary shapes and sizes, a boundary element method was also implemented to calculate the radiation force and torque acting on rigid spheroids, ellipsoids, and cylinders in inviscid fluid [9]. While many studies have been devoted to the primary acoustic radiation force, few studies were specific to characterizing the interparticle or secondary radiation force. The interparticle or secondary radiation force was first studied by Bjerknes [10] for a pair of pulsating bubbles. After Bjerknes, many theoretical and experimental studies were conducted to estimate the interparticle radiation force. Among them, few are specific to the interest and related to the acoustic interaction. Embleton [11] showed theoretically that the interparticle radiation force between two rigid spheres decreases with the increasing center-to-center distance for the axisymmetric case where the center-to-center line is aligned in the incident wave direction. The interaction force was also shown to be repulsive for this configuration. The direction and magnitude of the interparticle radiation force between rigid spheres were also studied by Nyborg and Gershoy [12]. Crum [13] studied the interparticle radiation force between bubbles both

---
[*]Also at National University of Singapore (Suzhou) Research Institute, Suzhou, Jiangsu 215123, People's Republic of China; limkm@nus.edu.sg

experimentally and theoretically, showing that the magnitude of the interparticle radiation force increases with increasing size of the bubbles. Zheng and Apfel [14] investigated the interparticle radiation force for compressible spherical particles and derived an expression for the interparticle radiation force.

Elaborate theoretical and numerical models for the secondary radiation force have also been developed in recent years. Doinikov and Zavtrak [15] studied the interaction between bubbles using numerical models and multipole expansion. The study was subsequently extended to the interaction between compressible particles [16]. Silva and Bruus [17] and Sepehrirahnama *et al.* [18] presented the variation of interparticle radiation force between spherical particles with respect to the center-to-center distance of the particles. The effect of viscosity was further included by Sepehrirahnama *et al.* [19], showing that the magnitude of interparticle force increases in the presence of fluid viscosity. There are also studies where the interparticle radiation force has been measured from the experimental observations.

Recent experimental studies of the interparticle radiation force based on trajectory motion of particles in an acoustic field have also been reported by Woodside *et al.* [20], Garcia-Sabaté *et al.* [21], and Castro and Hoyos [22]. These studies consider the equation of motion of the particles, accounting for the added fluid-mass effect and inertia of the particle. Woodside *et al.* [20] estimated the relative order of magnitude between the secondary radiation force and the primary radiation force. Garcia-Sabaté *et al.* [21] used the abrupt change in the velocity of the particles as an indicator of the interparticle radiation force. The key parameter for calculation of the interparticle radiation force is attributed to the critical distance at which the abrupt change in the velocity occurs. Castro and Hoyos [22] conducted similar studies in microgravity conditions and compared the acoustic radiation forces observed at sea level and at microgravity conditions.

It has been difficult to measure the interparticle radiation force in experiments accurately and compare them to those predicted by theoretical and numerical models. Real-world experiments typically have complications, such as a large number of particles, viscous and thermal effects of the fluid, and wall boundary effects, that are usually not captured by simple models. In this study we demonstrate a methodology to experimentally quantify the interparticle radiation force between a pair of polystyrene microbeads in the Rayleigh limit ($ka \ll 1$). The pair of beads was carefully isolated from the rest of the bead-fluid suspension and the interaction between the pair of beads was continuously observed near the pressure node of an ultrasound standing wave in a microchannel. This scenario gives an accurate description of the interparticle force with minimum contribution from the primary radiation force and influence from the channel sidewalls [Fig. 1(b)] and other beads. Subsequently, a theoretical model was used to extract the interparticle radiation force, accounting for the fluid drag force present in the system. In contrast with previous studies [20–22], the present study neglects the inertia of the particle due to its small mass, but the hydrodynamic drag and interaction between the particles were included. The experimental procedure was also repeated several times on an isolated pair of beads to ensure consistency in the results. The

interparticle radiation force obtained in this study is of the same order of magnitude as the theoretical prediction, albeit larger in value. The force was also found to be attractive with the beads in close range in the pressure nodal plane of the standing wave, consistent with the theory [17,18].

II. METHODOLOGY

In this section we describe the experimental setup, sample preparation, and experimental procedure used in the present study to quantify the interparticle acoustic radiation force between two isolated spherical microbeads.

A. Experimental setup and procedure

A schematic of the experimental setup and the actual laboratory setup for the present study of the interparticle radiation force are shown in Figs. 1(a) and 1(b), respectively. The acoustofluidic device primarily consists of a microchannel mounted on a piezoelectric transducer. The microchannel is a ($400 \times 40 \ \mu m^2$)-cross-section Vitrocom glass capillary of 50 mm length and 40 μm wall thickness. The transducer was excited by a signal generator (Agilent 33120A) and high-speed bipolar amplifier (NF HSA 4101). The excitation frequency was chosen to be 1.875 MHz, corresponding to the resonance mode of the standing wave with half a wavelength across the channel width. The voltage and power input to the transducer were monitored through an oscilloscope (Hewlett-Packard 54600A) and a high-frequency multimeter (Agilent 3458A) connected to the amplifier output. Polystyrene microbeads dispersed in a water suspension were carefully injected into the microchannel in such a way that a pair of microbeads was isolated for experimental observation. Upon activation of the ultrasound standing wave, the trajectories of the microbeads were captured from the top of the channel by a CCD camera (Nikon) mounted on a microscope (Leica DMLM). An external light source (Leica CLS 150X) was used to illuminate the channel, while the fluorescent microbeads were observed by the blue light obtained from the excitation filter of the microscope. The temperature of the piezoelectric transducer was monitored using a 15 K Ω thermistor (MP-2444, TE Technology) to ensure that there was no significant temperature rise during the experiment.

Before every experiment run, the channel was rinsed thoroughly with water for 30 min at a flow rate of 5 ml/h. In a few specific cases, absolute ethanol was used to clean the channel surface, after which the channel was rinsed with water again. Once the microbeads were injected into the channel, the syringe was kept free and the specimens were allowed to settle in the channel before the valve was closed. The valve was used to prevent any fluid flow in the channel and also to reduce any pressure fluctuations from the environment during the experiment.

B. Specimen solution preparation

The experimental study of the interparticle radiation force was conducted for three different sizes of microbeads whose properties are given in Table I. Fluorescent polystyrene beads of nominal diameters 7.81, 9.9, and 12.32 μm were used. The beads typically come in an aqueous suspension of 2.5%
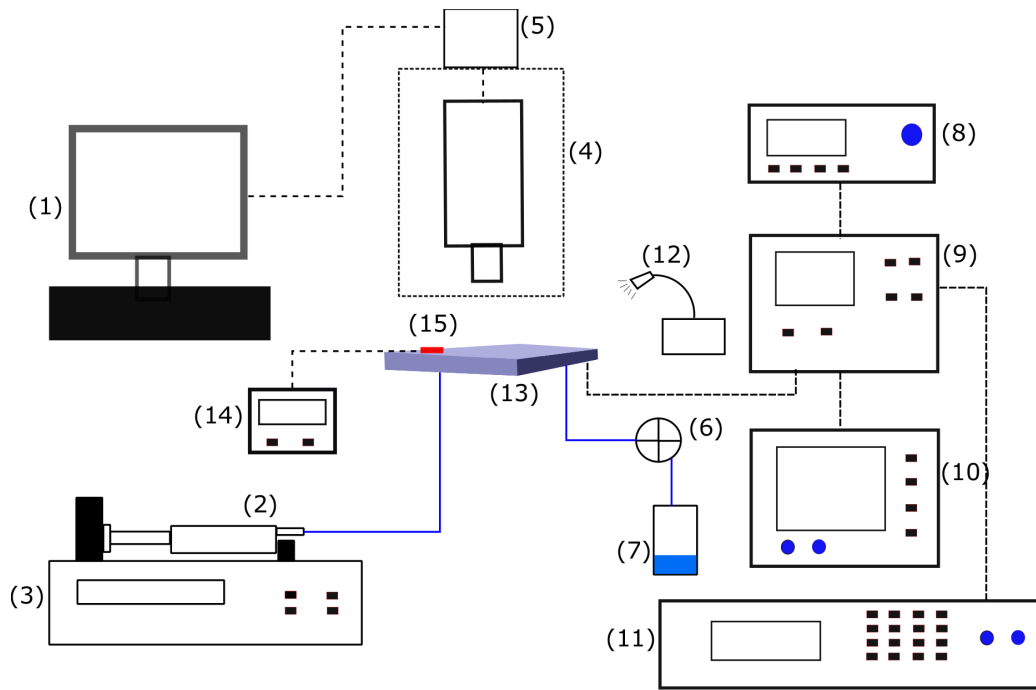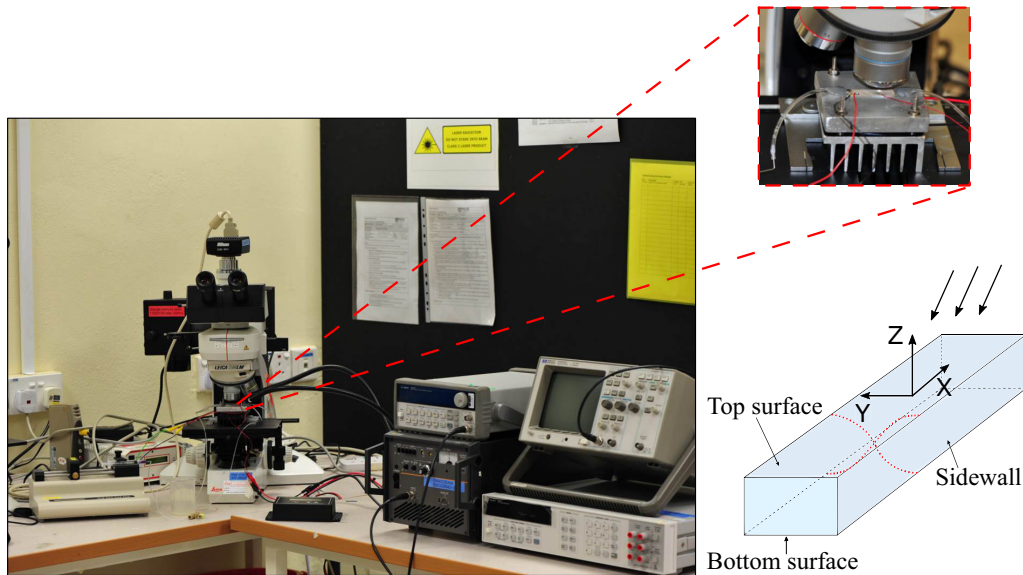
FIG. 1. (a) Schematic of the experimental setup: (1) computer, (2) syringe, (3) syringe pump, (4) microscope, (5) CCD, (6) valve, (7) waste flask, (8) signal generator, (9) amplifier, (10) oscilloscope, (11) multimeter, (12) light source, (13) microfluidic device, (14) temperature control unit, and (15) thermistor. (b) Laboratory setup for the acoustophoretic experiment [23].

TABLE I. Properties of the polystyrene beads used for the interparticle radiation force study with a density ρ_p of 1050 ± 2 kg m^{-3} [1,24] and compressibility β_p of $(2.25 \pm 0.18) \times 10^{-10}$ Pa^{-1} [1].

Mean diameter $2a$ (μm)	Standard deviation σ
7.81	0.11
9.9	0.5
12.32	0.1

(wt./vol %) concentration. To prepare the specimen solutions for experiment, the beads were diluted so that there are approximately 10–100 beads per microliter of the specimen solution. This low concentration of beads in the solution increases the chance of isolating and trapping just two beads in the observation region of the channel. Tween 20, a nonionic aqueous solution that prevents the beads from sticking to the channel wall, was further added to the solution at a volumetric ratio of 0.2%–0.3%.
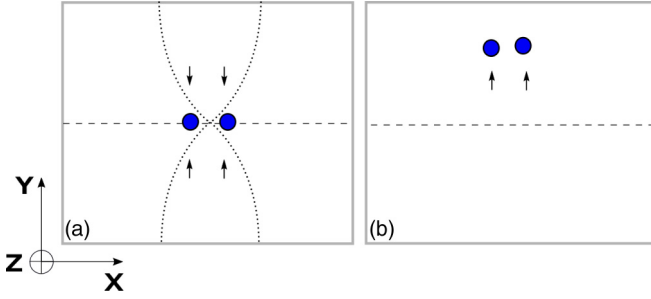
FIG. 2. Schematic of the microspheres at different excitation frequencies inside the channel: (a) 1.875 MHz and (b) 2.475 MHz [23]. The arrows indicate the direction of the radiation force.

C. Experimental procedure

During the experiment, a sine wave was generated with the signal generator at 6 V peak-peak voltage and the signal was further amplified ten times by the high-speed amplifier that drives the piezoelectric transducer. The frequency of the sine wave was first switched to 1.875 MHz and an ultrasound standing wave was set up across the width of the microchannel with the pressure node at the center of the channel [Fig. 2(a)]. The microbeads in the channel move towards the pressure nodal plane, getting in line with the pressure nodal plane as seen from the top of the channel. When the frequency of the sine wave was switched to 2.475 MHz, two pressure nodal planes were set up across the width of the channel away from the centerline. The beads were then pushed away from the center of the channel towards the wall of the channel as shown in Fig. 2(b). By switching between these two frequencies, the experiment can be repeated for the same pair of beads, pushing the beads towards and away from the centerline of the channel and capturing multiple observations of the bead trajectories. Nikon NIS Elements BR scientific image processing software was used to record the experimental observations as uncompressed color video (.avi) files at 15 frames/s. The interval between the sequential frames is approximately 0.06–0.11 s. The trajectories of the beads were then extracted from the media files using open source software (Tracker [25]) that gives the coordinates of the beads with respect to time. During the experiment, the temperature of the transducer was ensured to be between 22 °C and 25 °C. However, during the experimental observations of a pair of microbeads, the temperature fluctuated only within a small range of about 0.5 °C.

III. THEORETICAL MODEL

In order to calculate the interparticle radiation force between the pair of microbeads, a theoretical model was constructed for force interactions of the beads with the ultrasound standing wave, the host fluid, and between the two beads themselves. This section describes the formulations used for the acoustic radiation force, the hydrodynamic interaction, and the equations of motion corresponding to the trajectories of the beads.

A. Primary radiation force

Acoustic radiation force is due to the scattering of the acoustic wave from the particle or microbead. The primary radiation force is due to the interaction of a single particle with the incident wave. For the case of a microbead of radius a at a distance h from the pressure node in a standing wave, the time-averaged magnitude of the radiation force $\overline{\mathbf{F}}^P$ is given by [3]

$$\overline{F}^P = \tfrac{4}{3}\pi a^3 k E_{\mathrm{ac}}\varphi \sin(2kh), \tag{1}$$

where E_{ac} is the mean acoustic energy density of the resonating chamber, k is the wave number of the standing wave, and φ is the acoustic contrast factor. If $\varphi > 0$ the particles move to the pressure node (such as polystyrene beads in a water medium) and for $\varphi < 0$ the particles move to the pressure antinode (such as air bubbles in a water medium). The acoustic contrast factor φ is given by the expression

$$\varphi = \frac{5\rho_p - 2\rho_f}{2\rho_p + \rho_f} - \frac{\beta_p}{\beta_f}, \tag{2}$$

where ρ_p and ρ_f are the densities of the particle and the fluid medium, respectively, and β_p and β_f are the compressibilities of the particle and the fluid medium, respectively. The term $\overline{\mathbf{F}}^P$ is used to represent the nominal or mean primary radiation force in a uniform acoustic field of acoustic energy density E_{ac}.

However, the acoustic energy density in an actual experiment may not be uniform due to imperfections in the resonance chamber and the nonuniform transfer of energy from the piezoelectric transducer to the resonance chamber [20]. The spatial perturbations in the acoustic energy density will cause perturbations in the primary radiation force. Such perturbations in force are denoted by $\tilde{\mathbf{F}}_x^P$, $\tilde{\mathbf{F}}_y^P$, and $\tilde{\mathbf{F}}_z^P$ along the x, y, and z axes, respectively. Figure 3 shows the schematic of the components of the primary acoustic radiation force in Cartesian coordinate system. The standing wave is along the y axis and the pressure nodal plane is in the x-z plane. The $\tilde{\mathbf{F}}_{xz}^P$ is the resultant component of $\tilde{\mathbf{F}}_x^P$ and $\tilde{\mathbf{F}}_z^P$. This term $\tilde{\mathbf{F}}_{xz}^P$ is also known as the transverse component of the primary radiation force in the literature [20–22]. Due to the nonuniformity in
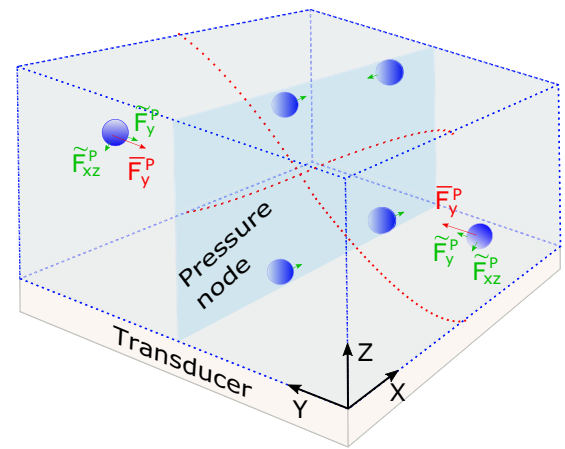

FIG. 3. Primary radiation force components on particles due to plane standing wave. Here $\overline{\mathbf{F}}_y^P$ (red arrow) is the nominal primary radiation force along the incident wave direction of the y axis. The perturbations in primary radiation force ($\tilde{\mathbf{F}}_{xz}^P$ in the transverse plane x-z and $\tilde{\mathbf{F}}_y^P$ along the y axis) due to the nonuniformity of the acoustic energy density are indicated by green arrows [23].

the energy density, the suspended beads in the fluid may form clusters instead of a pearl chain in the pressure nodal plane.

Hence, the primary radiation force can be written in two parts: (a) a nominal force part due to the mean acoustic energy (assumed uniform) in the chamber and (b) a perturbation part due to nonuniformity in the acoustic energy. For the standing wave used in the experiment, the nominal part of the primary radiation force acts only in the y direction, as denoted by $\overline{\mathbf{F}}_y^P$; the nominal part of the force does not have x and z components. The total primary radiation force is then expressed as

$$\mathbf{F}^P = \overline{\mathbf{F}}_y^P + \tilde{\mathbf{F}}_x^P + \tilde{\mathbf{F}}_y^P + \tilde{\mathbf{F}}_z^P. \tag{3}$$

B. Secondary radiation force

The secondary radiation force or interparticle radiation force is due to the scattered field from a nearby particle. To illustrate this, consider a target sphere at a distance r from the source sphere of the scattered field. The total field at the location of the target sphere is given by $\Phi = \Phi_{\text{in}} + \Phi_s$, as illustrated in Fig. 4. In this scenario, the target sphere experiences the primary radiation force $\mathbf{F}^P$ due to the incident field Φ_{in} and the interparticle radiation force or the secondary radiation force $\mathbf{F}^s$ due to scattered field Φ_s from the source sphere. The interparticle radiation force $\mathbf{F}^s$ can be decomposed into two components: (a) a radial component $\mathbf{F}_r^s$ acting along the line connecting the centers of the spheres and (b) a tangential component $\mathbf{F}_\theta^s$ perpendicular to e_r. The sign of the radial component of interparticle radiation force changes as θ changes from 0 to $\pi/2$ [18]. At the pressure nodal plane ($\theta = \pi/2$), the interparticle radiation force was reported to act only in the radial direction and the force is attractive [18].

C. Hydrodynamic interaction between two translating spheres

A translating sphere in a fluid medium induces flow in the medium. The induced flow is responsible for the hydrodynamic interaction between the two moving particles. For a sphere of radius a translating with velocity U_i in an infinite quiescent
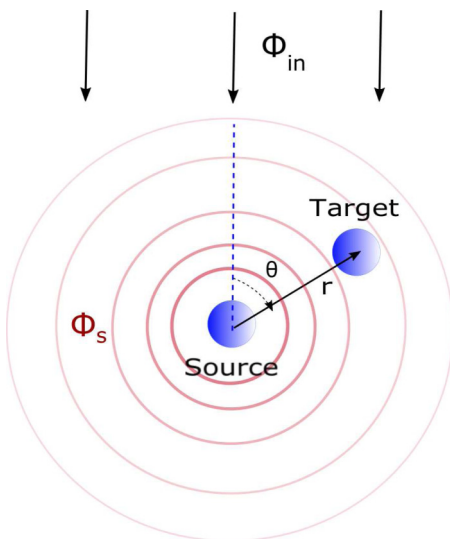
FIG. 4. Schematic of the scattered field from a suspended sphere in the fluid [23].
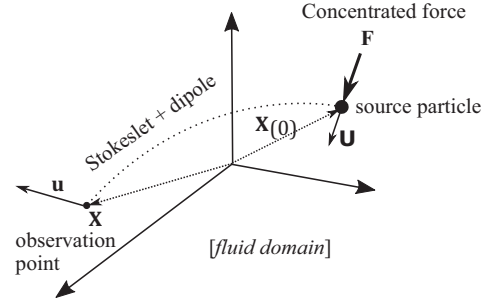
FIG. 5. Schematic of induced flow through the Stokeslet and the potential dipole due to a concentrated force acting on a translating sphere in the fluid domain [23].

fluid of dynamic viscosity μ, an external force F_i is needed to sustain that motion. The relationship between the velocity and the external force is given by

$$U_i = \frac{F_i}{6\pi\mu a}. \tag{4}$$

The induced flow in the surrounding fluid due to this translating sphere is represented by the Stokeslet and the potential dipole centered at the translating sphere [26] (Fig. 5). Therefore, by knowing the concentrated force acting on the sphere at $\mathbf{x}_{(0)}$, the induced flow at a point $\mathbf{x}$ in the fluid domain outside the sphere can be calculated using

$$u_i(\mathbf{x}) = \left(\frac{\delta_{ij}}{r} + \frac{\hat{x}_i \hat{x}_j}{r^3} \right) g_j + \left(-\frac{\delta_{ij}}{r^3} + 3\frac{\hat{x}_i \hat{x}_j}{r^5} \right) d_j, \tag{5a}$$

where

$$g_j = \tfrac{3}{4} a U_j, \quad d_j = -\tfrac{1}{4} a^3 U_j. \tag{5b}$$

Here δ_{ij} is the Kronecker delta, $r = |\mathbf{x} - \mathbf{x}_{(0)}|$, and U_j is the velocity of the translating sphere given by Eq. (4).

For the case with two spheres (each of radius a) at two different locations 1 and 2, subjected to external forces $F_{i(1)}$ and $F_{i(2)}$, respectively, the velocity of each sphere may be determined by considering one force at a time and then superposing the results together. If only $F_{i(1)}$ is acting on the system, the velocities of the spheres, $U_{i(1|1)}$ and $U_{i(2|1)}$ at locations 1 and 2, are given by

$$\begin{pmatrix} U_{i(1|1)} \\ U_{i(2|1)} \end{pmatrix} = \frac{1}{6\pi\mu a} \begin{pmatrix} \delta_{ij} \\ C_{ij} \end{pmatrix} F_{j(1)}, \tag{6}$$

where the components of the matrix C_{ij} are given by the coefficients in Eq. (5). Similarly, if only $F_{i(2)}$ is acting on the system, the velocities $U_{i(1|2)}$ and $U_{i(2|2)}$ at locations 1 and 2 are given by

$$\begin{pmatrix} U_{i(1|2)} \\ U_{i(2|2)} \end{pmatrix} = \frac{1}{6\pi\mu a} \begin{pmatrix} C_{ij} \\ \delta_{ij} \end{pmatrix} F_{j(2)}. \tag{7}$$

By the principle of superposition, the total velocities of the spheres at 1 and 2 due to both external forces $F_{i(1)}$ and $F_{i(2)}$ are given by

$$\begin{pmatrix} U_{i(1)} \\ U_{i(2)} \end{pmatrix} = \frac{1}{6\pi\mu a} \begin{bmatrix} \delta_{ij} & C_{ij} \\ C_{ij} & \delta_{ij} \end{bmatrix} \begin{pmatrix} F_{j(1)} \\ F_{j(2)} \end{pmatrix}. \tag{8}$$

For the case where the spheres only move in the x-y plane, the components of the matrix C_{ij} are given

explicitly by

$$C_{ij} = \frac{3a}{4r^5} \begin{bmatrix} r^4 + \frac{r^2 a^2}{3} + (r^2 - a^2)\hat{x}^2 & (r^2 - a^2)\hat{x}\hat{y} \\ (r^2 - a^2)\hat{x}\hat{y} & r^4 + \frac{r^2 a^2}{3} + (r^2 - a^2)\hat{y}^2 \end{bmatrix}, \tag{9}$$

where indices i and j are x or y. For the case where the inertia effects of the spheres are negligible (small mass or negligible acceleration), the external force will be equal and opposite to the fluid drag force acting on the spheres based on a quasistatic model

$$F_{i(1)} = -F_{i(1)}^D, \quad F_{i(2)} = -F_{i(2)}^D, \tag{10}$$

where F_i^D is the fluid drag force.

D. Two spheres in a standing wave

The present model is developed to represent the experimental observations of the pair of microbeads in a standing wave and to calculate the interparticle radiation force between the pair of microbeads. In the experiments, the observations were limited to the case where the center-to-center line of the beads is nearly perpendicular ($80° < |\theta| \leqslant 90°$) to the incident wave as they approach the pressure node. The beads are thus assumed to be at same distance from the pressure nodal plane, as shown in Fig. 6. Although the starting positions of the beads may be far from the pressure node, only the part of the trajectory (with snapshots taken from the video) near the pressure node ($h < 30\ \mu$m) is considered for the analysis. The analysis is also limited to those snapshots in which the beads are not in contact with each other.

First, the coordinates of the beads were extracted from the snapshots of the trajectories and fitted to a quadratic polynomial of time using the least-squares method. Next the velocities of the beads were calculated by differentiating the positions with respect to time. From the velocities of the beads, the fluid drag force acting on each bead can be calculated using Eqs. (8) and (10). Since the beads are very small compared to the channel size and the fluid in the channel is stationary, the infinite quiescent fluid assumption is valid. The inertia effect of the microbead is also negligible due to the small mass of the beads. This will be validated in Sec. IV by comparing the

inertia term to the external radiation force and fluid drag force using the data from the experiment.

As the beads are very close to each other, the perturbation part of primary radiation forces $\tilde{\mathbf{F}}_x^P$ and $\tilde{\mathbf{F}}_y^P$ due to the nonuniformity in the energy density is considered to be the same for both beads within that small region. The interparticle radiation force acts only along the center-to-center line or the x axis since the beads are nearly perpendicular to the wave direction ($80° < |\theta| \leqslant 90°$). The tangential component of the interparticle radiation force $\mathbf{F}_\theta^s$ is close to zero.

From the free-body diagram of each bead (Fig. 6), the equations of motion of each bead are written as follows:

$$\tilde{F}_x^P + F_r^s - F_{x(1)}^D = 0, \tag{11a}$$

$$-\overline{F}_{y(1)}^P - \tilde{F}_y^P + F_{y(1)}^D = 0, \tag{11b}$$

$$\tilde{F}_x^P - F_r^s - F_{x(2)}^D = 0, \tag{11c}$$

$$-\overline{F}_{y(2)}^P - \tilde{F}_y^P + F_{y(2)}^D = 0. \tag{11d}$$

The radiation forces in the x and y directions are fully decoupled. The interparticle radiation force F_r^s at every snapshot in time is given by $F_r^s = \frac{1}{2}(F_{x(1)}^D - F_{x(2)}^D)$, which is obtained by subtracting Eqs. (11a) and (11c). The fluid drag force components $F_{x(1)}^D$ and $F_{x(2)}^D$ are determined directly from the velocities of the two beads.

IV. RESULTS

In this section the interparticle radiation force between pairs of microbeads of diameters 7.81, 9.9, and 12.32 μm is presented. Each pair of beads has the same diameter, so the results are labeled by the diameter of each pair. First, the trajectories of the three pairs of beads (one pair for each diameter size) are presented as evidence of the interparticle radiation force. Subsequently, the interparticle force data are extracted and compared against the theory.

A. Experimental observations of bead trajectories

As the focal plane of the microscope is fixed in the vertical direction (z axis), clear and focused observations of the beads indicate that the beads were levitated to the same depth in the channel for the subsequent image analysis. The observed intensities of the beads in the image frames were also very close to each other. Due to the limitation of the experimental setup, the exact positions of the beads on the z axis could not be measured accurately during the experiment. However, when the ultrasound was switched off, the beads slowly settled downward in the channel, shown by a drop in intensity of the beads as the beads went out of focus. This also indicates that the beads were not sedimented in the channel during the observations but levitated in the midplane of the channel between the top and bottom surfaces when the ultrasound was switched on.
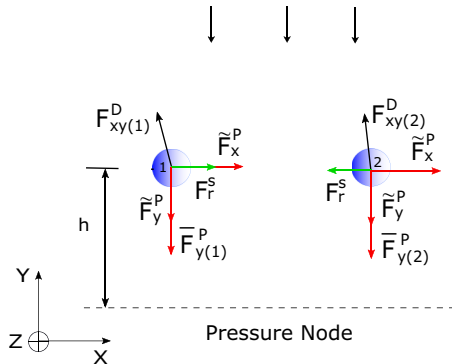

FIG. 6. Free body diagrams of the individual beads approaching the pressure node.
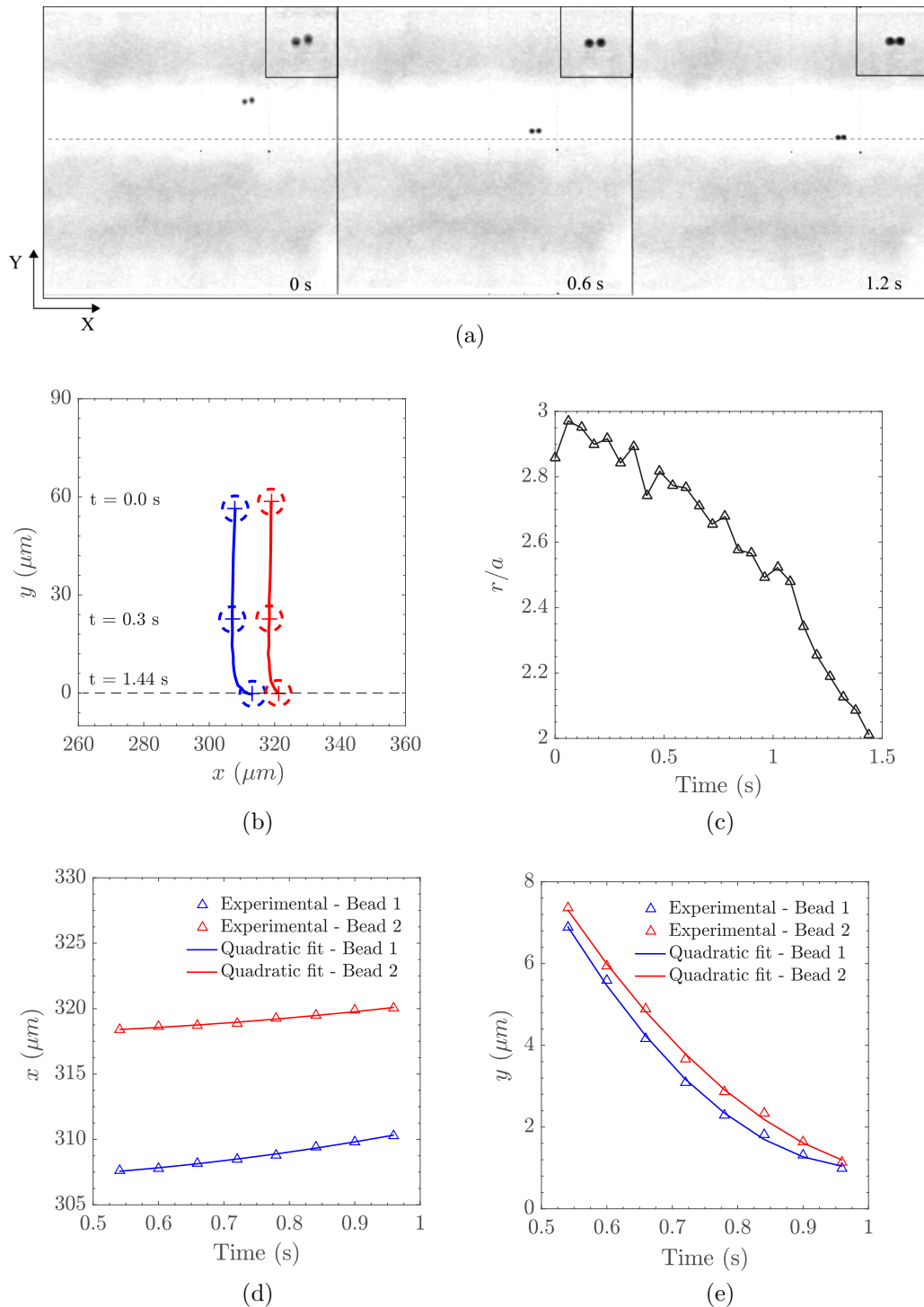
FIG. 7. Experimental observations of a pair of 7.81-μm polystyrene beads (first observation of pair 4 of 7.81-μm beads): (a) snapshots of the bead trajectory during the experiment, (b) trajectories of the two beads coming together on the x-y plane, (c) center-to-center distance, (d) x trajectories, and (e) y trajectories.

The levitation in the z direction is due to a weak standing wave across the channel height of 40 μm that has a corresponding resonance of 18.75 MHz. The presence of this frequency, which is an integer multiple of the excitation frequency of 1.875 MHz, is likely due to the slight nonlinearities in the setup of the channel and piezoelectric transducer.

Six to ten frames before the beads reached the pressure nodal plane were used for the trajectory estimation and analysis. There are more frames available for the analysis for 7.81-μm beads compared to 12.32-μm beads because the larger beads experience larger primary radiation force, hence reaching the pressure nodal plane faster. The x-y coordinates of each bead in
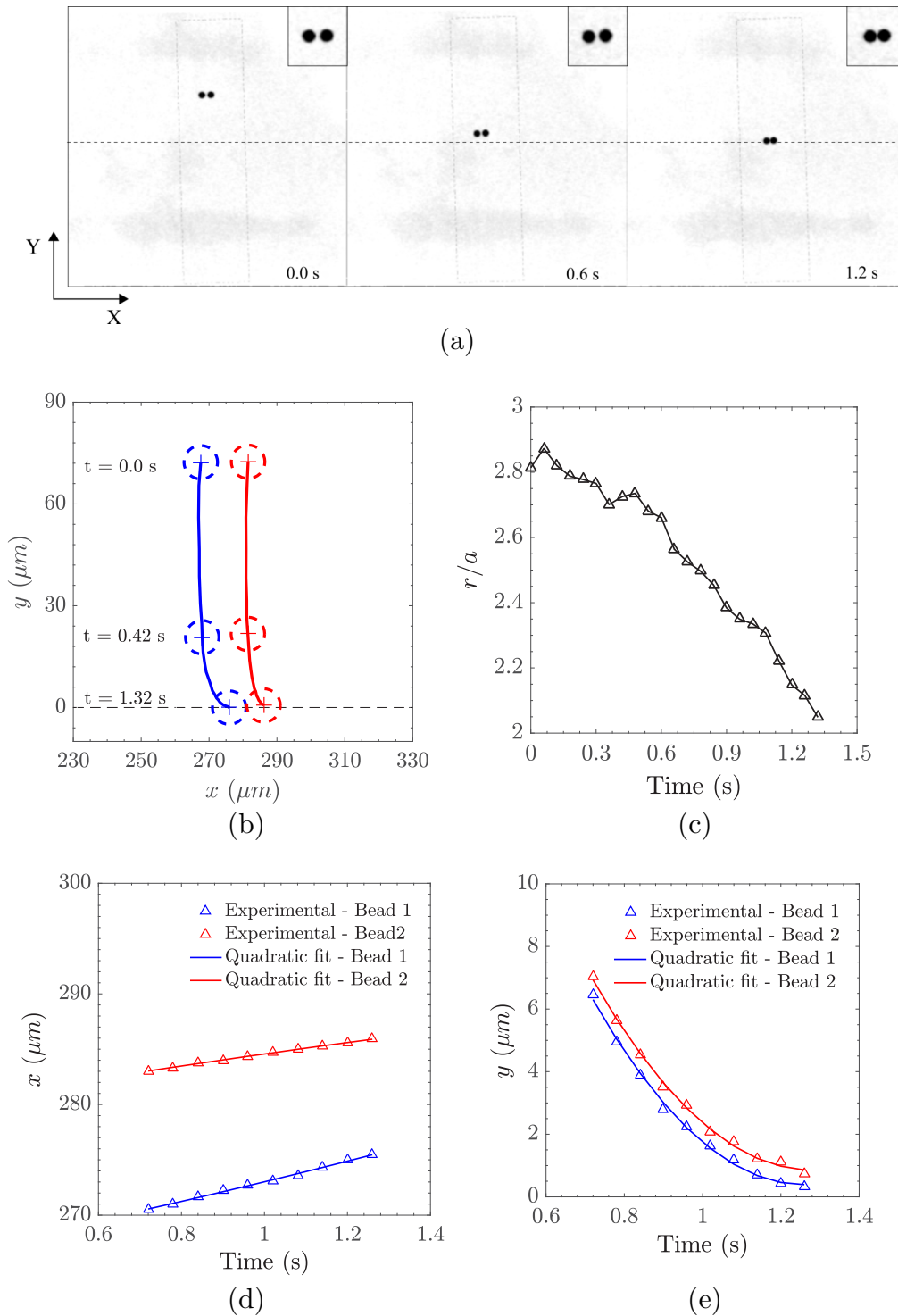
FIG. 8. Experimental observations of a pair of 9.9-μm polystyrene beads (second observation of pair 5 of 9.9-μm beads) [23]: (a) snapshots of the bead trajectory during the experiment, (b) trajectories of the two beads coming together on the x-y plane, (c) center-to-center distance, (d) x trajectories, and (e) y trajectories.

the snapshots were extracted and fitted by quadratic functions against time using the least-squares method, allowing the velocity of each bead to be obtained easily by differentiation of its coordinates with respect to time. From the velocity of the beads, the drag force on the beads was calculated from Eq. (8) and subsequently the interparticle force was calculated from Eq. (11).

Figures 7, 8, and 9 show the experimental observations for pair of 7.81-, 9.9-, and 12.32-μm-diam beads, respectively. The figures show the first observation of pair 4 of 7.81-μm beads, the second observation of pair 5 of 9.9-μm beads, and the first observation of pair 3 of 12.32-μm beads. Figures 7(a), 8(a), and 9(a) show the snapshots of the bead trajectory obtained during the experiment. From the snapshots it can be seen that the beads
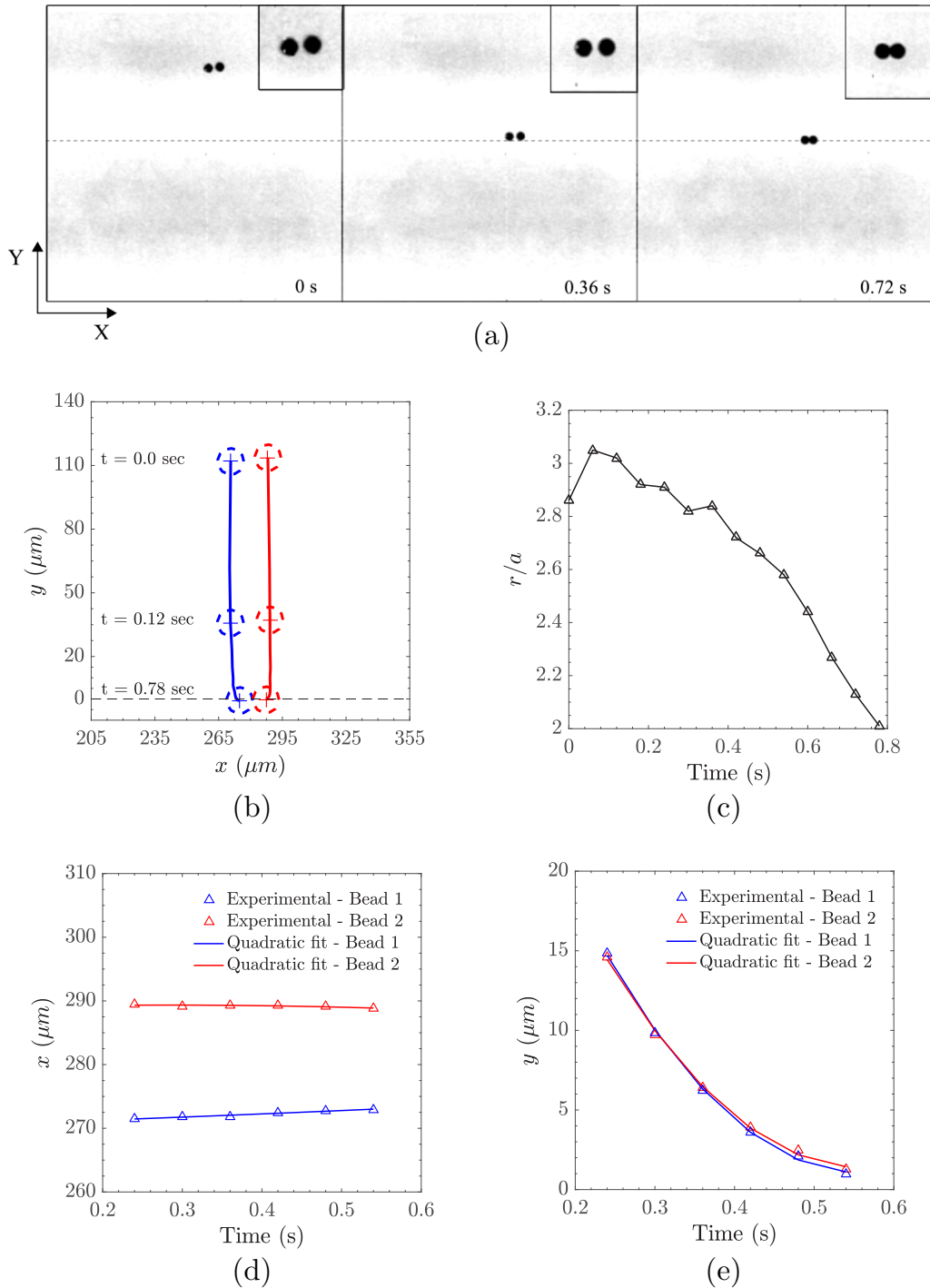
FIG. 9. Experimental observations of a pair of 12.32-μm polystyrene beads (first observation of pair 3 of 12.32-μm beads): (a) snapshot of the bead trajectory during the experiment, (b) trajectories of the two beads coming together on the x-y plane, (c) center-to-center distance, (d) x trajectories, and (e) y trajectories.

get closer as they approach the pressure nodal plane, indicating that there is an attractive force between them. In Figs. 7(b), 8(b), and 9(b) the trajectories of the two beads coming together are shown in the x-y plane. The experimentally measured center-to-center distance r against time for each case is plotted in Figs. 7(c), 8(c), and 9(c). The concave downward trend of the graph between the center-to-center distance against time is evidence of the attractive nature of the interparticle radiation

force which increases with decreasing center-to-center distance r. In Figs. 7(d), 8(d), and 9(d) and Figs. 7(e), 8(e), and 9(e), the respective x and y trajectories of the beads against time are presented. The triangular markers show the experimental observations and the solid line represents the quadratic fit using the least-squares method. From the free-body diagram (Fig. 6) it can be seen that bead 1 should move faster than bead 2 in the x direction when the interparticle radiation force is dominant.
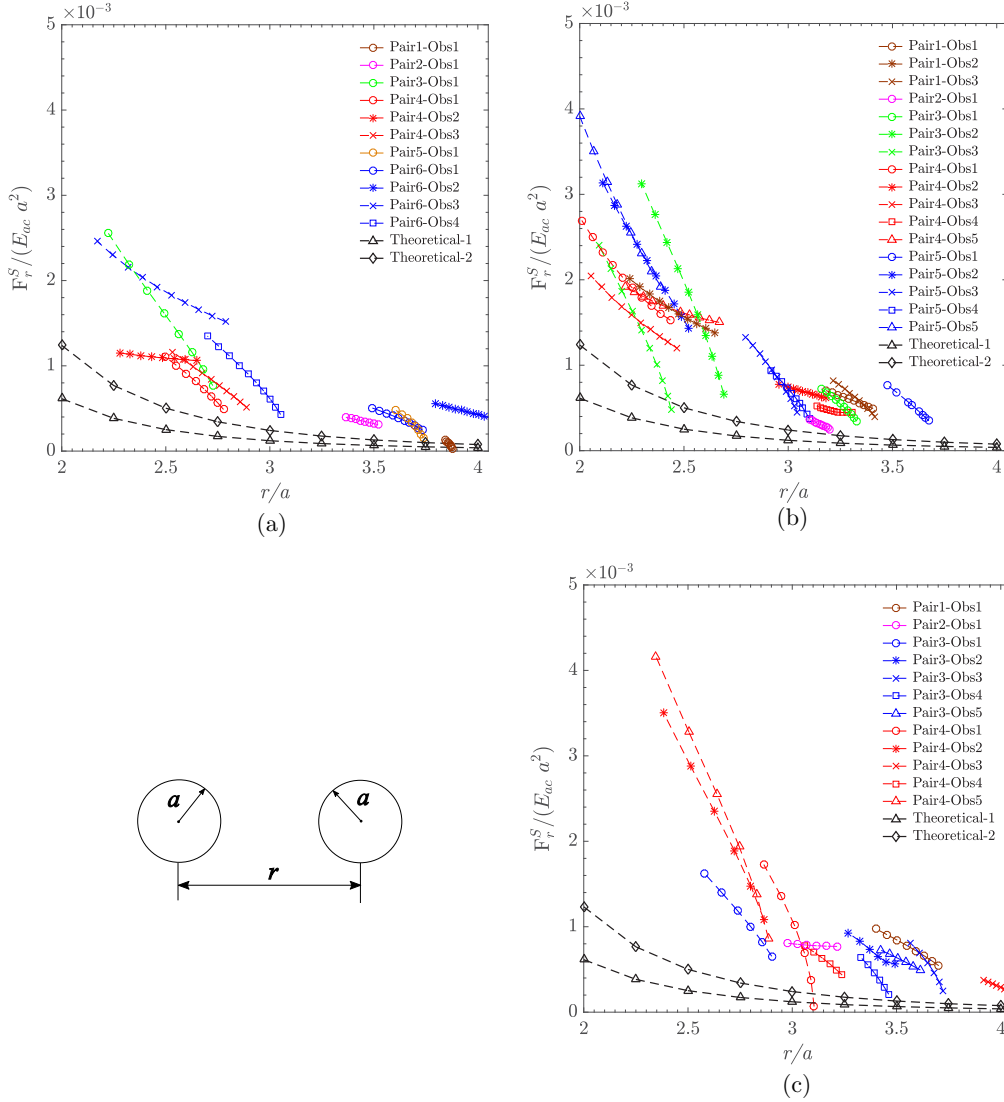
FIG. 10. Normalized interparticle radiation force $F_r^s/E_{ac}a^2$ with respect to the normalized center distance r/a between two equal-size polystyrene beads: (a) a pair of 7.81-μm polystyrene beads, (b) a pair of 9.9-μm polystyrene beads, and (c) a pair of 12.32-μm polystyrene beads. Theoretical-1 and Theoretical-2 refer to an analytical formula by Silva and Bruus [17] and a numerical simulation similar to that of Sepehrirahnama *et al.* [18], respectively.

This is evident from the increasing slope of the x trajectory for bead 1 (blue) and decreasing slope of the x trajectory for bead 2 (red) in Figs. 7(d), 8(d), and 9(d). Out of a total of 95 analyzed observations, 40 observations show the same trend with decreasing center-to-center distance r with the x trajectory, and the interparticle radiation force for these 40 observations is presented in the subsequent section. For the remaining cases, the observation of the interparticle radiation force between the particles was found to be erratic; this is probably due to environmental noise in the experimental setup and additional friction between the beads and the top surface of the capillary [Fig. 1(b)].

B. Comparison of interparticle force with theory

The data for the variation of interparticle radiation force F_r^s with respect to the center-to-center distance r for three different sizes of beads are extracted and plotted in Fig. 10.

The calculated interparticle radiation force F_r^s is normalized with respect to $E_{ac}a^2$, where E_{ac} is the acoustic energy density of the resonance chamber and a is the radius of the microbead. The acoustic energy density E_{ac} was estimated for each bead by observing the entire y trajectory of the bead and fitting it using the least-squares method with E_{ac} as the fitting parameter, using the method reported previously [1]. In this case with a pair of beads, the average of the two values of acoustic energy density from the two beads is used for the normalization. In this study the estimated energy density E_{ac} for all the observations is in the range of 7–18 J m^{-3}.

The experimental results on the interparticle force are compared with the theoretical predictions by Silva and Bruus [17] (shown as triangular markers for the Theoretical-1 curve) and Sepehrirahnama *et al.* [18] (shown as diamond markers for the Theoretical-2 curve). The theoretical results were obtained

for the case where the particles are in close range ($kr \ll 1$) at the pressure nodal plane (using $h = 0$) and the center-to-center line is perpendicular to incident wave ($\theta = \pi/2$).

The analytical expression by Silva and Bruus [17] for the calculation of the interparticle radiation force between two compressible spheres is given by

$$\mathbf{F}_r^s = -\pi k^4 E_{ac} a^6 f_1^2 \left\{ \frac{3}{(kr)^4} + O([kr]^{-2}) \right\} e_r, \qquad (12)$$

where e_r is the unit vector along the center-to-center line. The dipole scattering factor f_1 depends on the relative density between the particle and the host fluid and it takes a value of 0.0323 for polystyrene beads in water. For small center-to-center distances, only the first term in Eq. (12) is retained; by normalizing the force with $E_{ac} a^2$, the following simple approximation is obtained:

$$\frac{\mathbf{F}_r^s}{E_{ac} a^2} = -\pi f_1^2 \left\{ \frac{3}{(r/a)^4} \right\} e_r. \qquad (13)$$

The above theoretical relation between the normalized interparticle radiation force and the normalized center-to-center distance is plotted as the Theoretical-1 curve in Fig. 10. The Theoretical-2 curve is plotted based on a method similar to that of Sepehrirahnama et al. [18] with the compressibility of spheres included. The results were calculated numerically using higher multipole expansions up to fifth order, which is more accurate than the dipole approximation.

As shown in Fig. 10, the interparticle radiation force measured experimentally decreases with increasing center-to-center distance, consistent with the prediction by theory. However, the experimental results are larger than the theoretical estimates. It is also noted that the deviation between theory and experiment is larger when the beads get closer to each other and also for the larger beads. This suggests that the magnitude of interparticle radiation force is sensitive to the bead size ka. To further compare the results across the bead sizes, the interparticle radiation force for three different sizes of beads is plotted against the normalized center-to-center distance kr on a log-log scale in Fig. 11. The interparticle radiation force is normalized with respect to $E_{ac} k^4 a^6$ in this case. As shown in Fig. 11, the experimental results fall in a band which is above both theoretical predictions. The band of experimental results has a slope approximately equal to 4 in the log-log plot, which is in agreement with the prediction from theory, as given by the leading term in Eq. (12). The predictions from Sepehrirahnama et al. [18] (shown as the Theoretical-2 curve) are also closer to the experimental results, while the predictions from Eq. (12) based on just dipole approximation [17] are further away from the experimental results. This trend is consistent with the finding that when the beads are in close proximity, higher terms in multipole series expansion will give a better approximation of the interaction force, about two times greater than the dipole formulation [18]. Nonetheless, there is still a gap between the experimental results and the theory based on multipoles (the Theoretical-2 curve). This suggests that there are still some aspects of the interaction between the pair of beads that are not captured by the simple theoretical models.

Both theoretical models are based on the ideal fluid or inviscid theory. In the actual experiment, viscosity is present in the
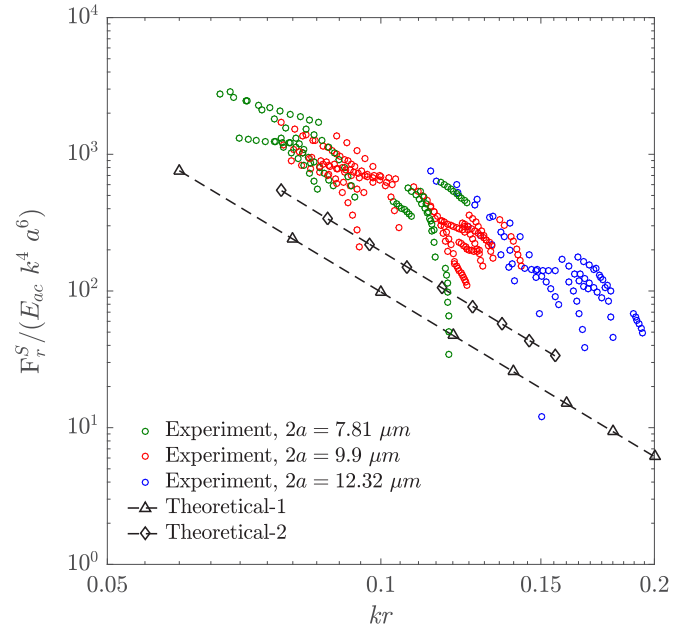

FIG. 11. Comparison of the interparticle radiation force across three different sizes of beads with the theoretical results. Theoretical-1 and Theoretical-2 refer to an analytical formula by Silva and Bruus [17] and a numerical simulation similar to that of Sepehrirahnama et al. [18], respectively.

water used as the host fluid. It is known that the viscosity will increase the interaction force between the two beads [19]. Also, acoustic streaming could be set up near the surface of the two beads and this will further affect the interaction between the beads. Another possible reason for the difference between the experimental and the theoretical interparticle radiation force F_r^s is likely the underestimation of acoustic energy density E_{ac} from the experiment. The microchannel used in the experiment is very shallow (40 μm); hence, the beads moving in the channel may experience the boundary layer effects from the top and bottom surfaces of the shallow channel. This will result in a greater fluid drag on the beads, which is underestimated by the simple Stokes drag formula written for an infinite fluid domain. With an appropriate correction factor applied to the Stokes drag, a larger acoustic energy density would be estimated which should be closer to the actual value in the experiment. This is further discussed in Sec. V. Nonetheless, the experimental results are of the same order of magnitude as the theoretical predictions and there are many other factors in the experiment that cannot be captured in simple theoretical models; we thus deem the experimental results and theoretical predictions to be in reasonable agreement.

C. Effects of bead inertia and hydrodynamic interaction

In the model developed in Sec. III to calculate the interparticle radiation force, the equations of motion for the beads were obtained with the quasistatic assumption. This assumes that the inertia force of the bead is negligible compared to the rest of the external force and fluid drag force. To validate this assumption, the inertia force of the beads is calculated from the experimental trajectories.

TABLE II. Comparison of the order of magnitude between the inertia force and the interparticle radiation force measured in the experiment; M is the mass of the bead and $\ddot{x}$ is the acceleration along the x axis.

Diameter (μm)	$\ddot{x}_{(max)}$ (m s^{-2})	$M\ddot{x}_{(max)}$ (N)	$F^s_{r(min)}$ (N)	Order of magnitude $M\ddot{x}_{(max)}/F^s_{r(min)}$
7.81	1.44×10^{-5}	3.76×10^{-18}	6.67×10^{-15}	10^{-3}
9.9	1.25×10^{-5}	6.68×10^{-18}	5.56×10^{-14}	10^{-4}
12.32	4.18×10^{-5}	4.29×10^{-17}	3.69×10^{-14}	10^{-3}

Table II gives a comparison of the inertia force, based on the measured acceleration of the bead from its trajectory, and the interparticle radiation force that is representative of external force acting in the system. The maximum observed acceleration of the beads along the x axis is on the order of 10^{-5} m s^{-2}. Taking into account the typical mass of the bead (approximately 10^{-13} kg), the inertia force is estimated to be on the order of 10^{-17}–10^{-18} N. This inertia force is about three order smaller than the smallest interparticle radiation force in the study. Hence, it is valid and justified that the inertia force be neglected in the equations of motion of the beads and a quasistatic model can be used. This is in agreement with the theory of the hydrodynamic interaction between particles at low Reynolds number. In theoretical calculations for low-Reynolds-number flow, the velocities of the interacting particles are expressed as the mobility matrix multiplied by the external force [27] and the inertia force is neglected.

In the model developed, the hydrodynamic interaction between the particles was explicitly introduced in calculating the fluid drag force on each bead. It is well known that the hydrodynamic interaction between the beads has a significant effect in the model. In order to illustrate this, the interparticle radiation force is recalculated using a model with only Stokes drag force acting on the bead and removing the hydrodynamic interaction term. This is equivalent to setting the coupling matrix **C** in Eq. (8) to zero or just using the Stokes formula (4) for the fluid drag force on each bead. The interparticle radiation force calculated from the experimental data without the hydrodynamic interaction is denoted by F^{s*}_r. This interparticle force F^{s*}_r is compared to our previous value F^s_r in Fig. 12, with the ratio F^{s*}_r/F^s_r plotted against the normalized center-to-center distance r/a of the beads. It can be seen that the ratio F^{s*}_r/F^s_r is always less than 1. This means that the interparticle radiation force calculated with consideration of the hydrodynamic interaction is greater than the case without hydrodynamic interaction. When the center-to-center distance is small, the interparticle radiation force will be underestimated by half if the hydrodynamic interaction is neglected. Hence, the hydrodynamic interaction is substantial in close range but its effect decreases as the center-to-center distance increases, as the ratio F^{s*}_r/F^s_r gets closer to 1 as the distance increases. For the investigation of the interparticle radiation force that is in very close proximity to the beads, the hydrodynamic interaction cannot be neglected from the total drag on the beads.

V. DISCUSSION

In this section the limitations in the model and likely sources of errors are discussed. The uncertainties in the calculations due to simplifications in the model are also estimated.

As mentioned in the preceding section, the shallow channel will result in a higher drag force, due to the top and bottom surfaces of the channel, compared to the Stokes drag formula. The correction factor to the Stokes drag formula for a sphere moving between two parallel planes can be calculated using the formulas given in Refs. [28,29]. The effect of two parallel planes on the overall drag depends on the diameter of the bead and the distance from the closest plane. The correction factor is largest for the 12.32-μm bead among the three sizes and is influenced most by the shallow channel. The values of the correction factor χ for a single 12.32-μm-diam bead are approximately equal to 1.42 and 1.65 at the middle of the channel and at the quarter height of the channel from the closest surface (top or bottom), respectively. So the calculated drag with the effect from the top and bottom surfaces will be
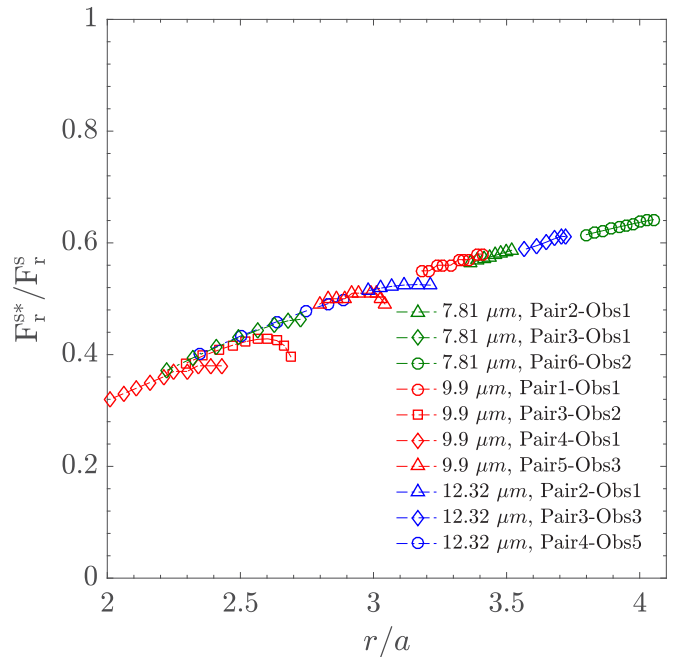

FIG. 12. Comparison of the interparticle radiation force with (F^s_r) and without (F^{s*}_r) hydrodynamic interaction for different pairs of beads.

approximately equal to 42% and 65% more than the Stokes drag for the above cases, respectively. Taking the channel height into consideration will lead to a higher estimate of E_{ac} and a larger interparticle radiation force in the final calculation due to the additive nature of the drag force. The results shown in Figs. 10 and 11 are normalized with respect to $E_{ac}a^2$ and $E_{ac}k^4a^6$, respectively. Considering the one-dimensional case of the beads moving along the centerline, the percentage change in the normalized experimental interparticle radiation force in Figs. 10 and 11 is given by $-c(1 - 1/\chi) \times 100\%$, where c is the off-diagonal element of the 2×2 mobility matrix in Eq. (8). As $0 < c < 1$ and $\chi > 1$, the percentage change is always negative. Therefore, with the extra drag due to the top and bottom surfaces, the deviation between the experimental results and the theoretical predictions in Figs. 10 and 11 will decrease. The percentage change depends on c (a function of center-to-center distance r/a) and χ (a function of the ratio of the bead radius to height of the channel). For a fixed value of χ, the percentage change in the experimental result decreases, as c decreases with increasing r/a. So the change in the experimental results in Figs. 10 and 11 will be noticeable when r/a is small. In the case of 12.32-μm beads at a distance $r/a = 2.26$ and with the beads at the midplane between the top and bottom surfaces, the percentage decrease in the normalized experimental result is approximately equal to 18%. However, the correction to the results given in Figs. 10 and 11 will be less than 18% for the rest of the larger interparticle distance r/a.

In the present study the model for hydrodynamic interaction calculation uses a Stokeslet and a potential dipole. To gauge the accuracy of this approximation, we compare the current results with an exact solution that used the full multipole expansion, as given in [28]. For the case of two equal-size spheres moving with equal velocities along the line of centres, with center-to-center distance $r/a = 2.26$, the difference in the two formulations is approximately equal to 6.96%. The difference drastically reduces to approximately 3.19% and approximately 0.89% at $r/a = 3.09$ and 4.70, respectively. Hence, we deemed the current model to provide a good approximation without excessive computations as needed for higher-order multipoles. The accuracy of the current model can certainly be improved when more terms are used from the multipole expansion. For spheres that are nearly touching, there will be additional lubrication effects as mentioned in Ref. [27]. The lubrication effect causes extra resistance and prevents the spheres from touching [27], indicating that the lubrication effect in the near field will further increase the interparticle radiation force.

Rayleigh streaming may also affect the dynamics of the particles in acoustophoresis [29,30]. In this case, the Rayleigh streaming will be due to the top and bottom surfaces of the channel resulting in streaming velocities in the channel width (y) and thickness (z) directions. The z component of the streaming velocity is smaller than the y component and it is insignificant in the region of observation between the sidewalls of the channel and the pressure node plane. Hence, the y component of the streaming velocity (in the channel width direction) will have a dominant effect on the particle dynamics. The effect of the Rayleigh streaming also depends on the particle size, which is more significant for smaller particles. With consideration of the y component of the Rayleigh streaming velocity [29] near the top or bottom

surface of the channel, the estimated acoustic energy density E_{ac} will be increased approximately by 6.7%, 4.2%, and 2.7% for 7.81-, 9.9-, and 12.32-μm beads, respectively. This y component of the Rayleigh streaming velocity can be added to the total drag force calculation. However, the mobility matrix in Eq. (8) is symmetric and the Rayleigh streaming will have no effect on the interparticle radiation force calculation from the experiment, as the interparticle force is in the x direction (along the channel length). Apart from Rayleigh streaming, there will be viscous streaming at the surfaces of the beads. In the previous study [19], it was shown that including viscous streaming in the theoretical model will result in a large interparticle radiation force. Although the theoretical study was shown for the axisymmetric layout of the beads with respect to the standing wave, it is expected that the viscous streaming at the beads' surfaces will contribute to a larger interparticle radiation force.

In the microfluidic experiments, there are also factors like the effects of temperature and Brownian motion. During the experiment, the signal generator was operated at a low excitation voltage (6 V peak to peak) and the change in temperature was observed to be within the range of approximately 0.5 °C. Hence, the effect of temperature is negligible. As the particles used are of micron size, the effect of Brownian motion is also insignificant in this study.

Furthermore, the variations in the density and compressibility of the beads will contribute to the uncertainty in the acoustic contrast factor φ and the dipole scattering factor f_1. This results in uncertainties of $\pm 8.4\%$ and $\pm 0.4\%$ in φ and f_1, respectively. Subsequently, the estimation of acoustic energy density E_{ac} and the calculation of interparticle radiation force (the Theoretical-1 curve [17]) will have uncertainties of $\pm 8.4\%$ and $\pm 9.2\%$, respectively.

VI. CONCLUSION

In this paper the interparticle radiation force or the secondary radiation force between a pair of beads in a standing wave was obtained experimentally. This was based on the observations of the trajectories of an isolated pair of beads in close proximity and approaching each other near the pressure nodal plane of the standing wave. As the beads approach the pressure nodal plane with their center-to-center line nearly perpendicular to the incident wave, the primary radiation force acting on both beads is negligible, allowing us to draw out the effects of the secondary radiation force. With a simple two-bead model, taking into account the hydrodynamic interaction force between the beads, the interparticle or secondary radiation force between the beads was calculated from the experimental trajectories. The experimental results on the interparticle radiation force show the expected trend of decreasing magnitude with interparticle distance. The results are of the same order of magnitude as the theoretical predictions, albeit two to four times larger in value compared to the theory. The results also show that the interparticle radiation force increases with increasing size of the particle. Finally, it was shown that the hydrodynamic interaction between the microbeads is substantial in close proximity and cannot be neglected in the model when we are investigating the short-range interparticle radiation force.

[1] D. Hartono, Y. Liu, P. L. Tan, X. Y. S. Then, L.-Y. L. Yung, and K.-M. Lim, On-chip measurements of cell compressibility via acoustic radiation, Lab Chip **11**, 4072 (2011).

[2] L. V. King, On the acoustic radiation pressure on spheres, Proc. R. Soc. London Ser. A **147**, 212 (1934).

[3] K. Yosioka and Y. Kawasima, Acoustic radiation pressure on a compressible sphere, Acta Acust. United Acust. **5**, 167 (1955).

[4] A. A. Doinikov, Proc. R. Soc. London A **447**, 447 (1994).

[5] A. A. Doinikov, Acoustic radiation pressure on a compressible sphere in a viscous fluid, J. Fluid Mech. **267**, 1 (1994).

[6] M. Settnes and H. Bruus, Forces acting on a small particle in an acoustical field in a viscous fluid, Phys. Rev. E **85**, 016327 (2012).

[7] S. Sepehrirahnama, F. S. Chau, and K.-M. Lim, Numerical calculation of acoustic radiation forces acting on a sphere in a viscous fluid, Phys. Rev. E **92**, 063309 (2015).

[8] K. A. Johnson, H. R. Vormohr, A. A. Doinikov, A. Bouakaz, C. W. Shields IV, G. P. López, and P. A. Dayton, Experimental verification of theoretical equations for acoustic radiation force on compressible spherical particles in traveling waves, Phys. Rev. E **93**, 053109 (2016).

[9] F. B. Wijaya and K.-M. Lim, Numerical calculation of acoustic radiation force and torque acting on rigid non-spherical particles, Acta Acust. United Acust. **101**, 531 (2015).

[10] V. F. K. Bjerknes, *Fields of Force* (Cornell University Library, Ithaca, 1906).

[11] T. F. W. Embleton, Mutual interaction between two spheres in a plane sound field, J. Acoust. Soc. Am. **34**, 1714 (1962).

[12] W. L. Nyborg and A. Gershoy, *Proceedings of the Second World Congress of Ultrasonics in Medicine* (Excerpta Medica, Amsterdam, 1973), pp. 360–366.

[13] L. A. Crum, Bjerknes forces on bubbles in a stationary sound field, J. Acoust. Soc. Am. **57**, 1363 (1975).

[14] X. Zheng and R. E. Apfel, Acoustic interaction forces between two fluid spheres in an acoustic field, J. Acoust. Soc. Am. **97**, 2218 (1995).

[15] A. A. Doinikov and S. T. Zavtrak, Radiation forces between two bubbles in a compressible liquid, J. Acoust. Soc. Am. **102**, 1424 (1997).

[16] A. A. Doinikov, Acoustic radiation interparticle forces in a compressible fluid, J. Fluid Mech. **444**, 1 (2001).

[17] G. T. Silva and H. Bruus, Acoustic interaction forces between small particles in an ideal fluid, Phys. Rev. E **90**, 063007 (2014).

[18] S. Sepehrirahnama, K.-M. Lim, and F. S. Chau, Numerical study of interparticle radiation force acting on rigid spheres in a standing wave, J. Acoust. Soc. Am. **137**, 2614 (2015).

[19] S. Sepehrirahnama, F. S. Chau, and K.-M. Lim, Effects of viscosity and acoustic streaming on the interparticle radiation force between rigid spheres in a standing wave, Phys. Rev. E **93**, 023307 (2016).

[20] S. M. Woodside, B. D. Bowen, and J. M. Piret, Measurement of ultrasonic forces for particle-liquid separations, AIChE J. **43**, 1727 (1997).

[21] A. Garcia-Sabaté, A. Castro, M. Hoyos, and R. González-Cinca, Experimental study on inter-particle acoustic forces, J. Acoust. Soc. Am. **135**, 1056 (2014).

[22] L. A. Castro and M. Hoyos, Determination of the secondary Bjerknes force in acoustic resonators on ground and in microgravity conditions, Microgravity Sci. Technol. **28**, 11 (2016).

[23] A. R. Mohapatra, Study of particle manipulation by acoustophoresis in microfluidics, M.Eng. thesis, National University of Singapore, 2016.

[24] M. D. Allen and O. G. Raabe, Slip correction measurements of spherical solid aerosol particles in an improved Millikan apparatus, Aerosol Sci. Technol. **4**, 269 (1985).

[25] Tracker, video analysis and modeling tool, http://physlets.org/tracker/ (accessed on 29 September 2017).

[26] C. Pozrikidis, *Boundary Integral and Singularity Methods for Linearized Viscous Flow* (Cambridge University Press, Cambridge, 1992).

[27] L. Durlofsky, J. F. Brady, and G. Bossis, Dynamic simulation of hydrodynamically interacting particles, J. Fluid Mech. **180**, 21 (1987).

[28] J. Happel and H. Brenner, *Low Reynolds Number Hydrodynamics: With Special Applications to Particulate Media* (Springer Science + Business Media, New York, 1983), Vol. 1.

[29] R. Barnkob, Physics of microparticle acoustophoresis: Bridging theory and experiment, Ph.D. thesis, DTU Nanotech, 2012.

[30] Lord Rayleigh, On the circulation of air observed in Kundt's tubes, and on some allied acoustical problems, Proc. R. Soc. London **36**, 10 (1883).